Identification of potent HSV antivirals using 3D bioprinted human skin equivalents

S. Tori Ellison[1†], Ian Hayman[2†], Kristy Derr[1], Paige Derr[1], Shayne Frebert[1], Zina Itkin[1], Min Shen[1], Anthony Jones[2], Wendy Olson[2], Lawrence Corey[2, 3], Anna Wald[2, 3, 4, 5], Christine Johnston[2, 3, 4], Youyi Fong[3], Marc Ferrer[1*], Jia Zhu[2, 3*]

[1]Department of Preclinical Innovation, National Center for Advancing Translational Sciences, National Institutes of Health; Rockville, Maryland 20850, USA.

[2]Department of Laboratory Medicine and Pathology, [4]Medicine, [5]Global Health, University of Washington; Seattle, WA 98195, USA.

[3]Vaccine and Infectious Disease Institute, Fred Hutchinson Cancer Research Center; Seattle, WA 98109, USA.

*Corresponding Author Email: marc.ferrer@nih.gov; jiazhu@uw.edu

† These authors contributed equally to this work

One Sentence Summary: High-throughput screen using 3D bioprinted human skin equivalents to identify antivirals against HSV and evaluate cell-type specific effects.

Abstract:

Herpes simplex virus (HSV) infection has worldwide public health concerns and lifelong medical impacts. The standard therapy, acyclovir, has limited efficacy in preventing HSV subclinical virus shedding, and drug resistance occurs in immunocompromised patients, highlighting the need for novel therapeutics. HSV infection manifests in the skin epidermal layer, but current drug discovery utilizes Vero cells and fibroblasts monolayer cultures, capturing neither *in vivo* relevance nor tissue environment. To bridge the gap, we established 3D bioprinted human skin equivalents that recapitulate skin architecture in a 96-well plate format amenable for antiviral screening and preclinical testing. Screening a library of 738 compounds with broad targets and mechanisms of action, we identified potent antivirals, including most of the known anti-HSV compounds, validating the translational relevance of our assay. Acyclovir was dramatically less potent for inhibiting HSV in keratinocytes compared to donor-matched fibroblasts. In contrast, antivirals against HSV helicase/primase or host replication pathways displayed similar potency across cell types and donor sources in 2D and 3D models. The reduced potency of acyclovir in keratinocytes, the primary cell type encountered by HSV reactivation, helps explain the limited benefit acyclovir and its congeners play in reducing sexual transmission. Finally, we demonstrated that our 3D bioprinted skin platform can integrate patient-derived cells, facilitating the incorporation of variable genetic backgrounds early into drug testing. Thus, these data indicate that the 3D bioprinted human skin equivalent assay platform provides a more physiologically relevant approach to identifying potential antivirals for HSV-directed drug development.

Introduction

Herpes simplex virus type 1 (HSV-1) and type 2 (HSV-2) cause recurrent oral and genital ulcer diseases and infect two-thirds of the global population (1, 2). Both HSV-1 and HSV-2 can cause neonatal herpes with high mortality and devastating neurological impairment (3, 4). HSV-2 infection increases the risk of human immunodeficiency virus (HIV) acquisition (5-8), with a recent study estimating 420,000 of 1.4 million newly acquired HIV infections annually attributable to HSV-2 infection (9). Despite successes in animal studies, candidate HSV-2 vaccines faltered in human trials (10-13). Acyclovir, the primary treatment for HSV infection, alleviates disease severity and shortens outbreak duration (14, 15) but faces drug resistance in immunocompromised patients (16-18), limited efficacy in preventing subclinical reactivation, (19) and fails to address the increased risk of HIV transmission (8, 20, 21). Thus, novel therapeutic strategies and antiviral agents are needed to address the public health burden of HSV infection.

Drug development relies heavily on 2D monolayers and animal models to assess drug safety and efficacy. Conventional *in vitro* cultured monolayers facilitate rapid and robust infectivity assays but don't recapitulate complex cell-cell and cell-matrix interactions reflective of native tissues (22, 23). Consequently, these cellular assays often fail to predict drug responses in humans accurately (24). Animal models lack the predictive value and biological relevance to humans for effective drug discovery and development (25-27). This dilemma is evident in drug candidates failing to progress from Phase I to Phase III clinical trials, resulting in continued high costs for developing new pharmaceuticals (28-30). 3D *in vitro* models closely mimicking human tissues and organs offer opportunities to circumvent the limitations in clinical predictability of current drug R&D platforms (31, 32).

Bioengineered tissues bridge the gap between existing cellular and animal models and the complexity of human hosts and offer a powerful platform for expediting drug discovery, toxicity screening, and preclinical testing in a high-throughput, cost-effective manner (24). These *in vitro* human tissue models are designed to replicate key features of *in vivo* organs, such as cell type composition, 3D microarchitecture, functional tissue interfaces, and

organ-specific microenvironments (33). They offer unique opportunities for real-time visualization and high-resolution analysis of biological processes often unattainable in simpler cellular and animal models.

Skin and mucosal barriers are the primary tissue of concern for HSV initial infection and recurrent viral replication following reactivation. Skin tissue comprises the epidermis, dermis, and subcutaneous layer, forming a physical barrier protecting against pathogens and harmful environmental substances (34). The epidermis primarily consists of keratinocytes, which can differentiate into stratified layers, from the innermost stratum basale to the outmost stratum corneum. Human biopsy studies of recurrent HSV infection indicate basal keratinocytes at the dermal-epidermal junction (DEJ) serve as the replication targets for HSV reactivation through sensory nerve innervation and neurite extension into DEJ (35, 36). Our recently developed 3D skin-on-chip also demonstrated that basal keratinocytes were the most susceptible targets for HSV infection during keratinocyte differentiation (36). Thus, both *in vivo* and *in vitro* evidence highlight the importance of using multicellular tissue models that recapitulate skin architecture when developing HSV therapeutics.

Skin tissue equivalents consisting of keratinocytes and fibroblasts have been developed to study human diseases and drug toxicity (37-39). We developed bioprinted human skin equivalents (HSE) that differentiate into a stratified epidermis at the air-liquid interface (ALI) (40, 41). Here, we implemented a high-throughput screen (HTS) using 3D bioprinted HSE in a 96-well format and leveraging HSV-GFP reporter virus with high-content imaging. Our 3D bioprinted assay platform identified potent antiviral compounds, including 23 known anti-HSV candidates. We selected 11 compounds to evaluate in adult human skin-derived keratinocytes and fibroblasts, uncovering pharmacological properties distinct among cellular types in 2D and 3D, thus highlighting the importance of applying physiologically relevant assays in drug discovery and development.

RESULTS

2.1 Development of HSV Infection Assays on 3D Bioprinted Human Skin Equivalents

To create physiologically relevant *in vitro* human skin models of HSV-1 infection for antiviral screening, we 3D bioprinted HSE in a 96-transwell plate format (40). Neonatal human fibroblasts were suspended in a hydrogel containing gelatin, collagen, and fibrin, loaded into a glass syringe, then bioprinted onto the apical side of a 96 transwell insert using a plunger-based 3D bioprinter (Fig. 1A). After 7 days of maturation, neonatal human keratinocytes were pipetted on top of each dermal tissue and submerged in epidermalization media for another 7 days (42). To induce keratinocyte differentiation and epidermis stratification, the tissues were lifted to ALI using a custom 3D printed adaptor (fig. S1) and cultured in cornification media at the basal surface of the dermis for 7 days (Fig. 1A) (40-42). Hematoxylin and eosin (H&E) staining confirmed that ALI cultures produced HSE with a dermis and differentiated epidermis, including a stratum basale and stratum corneum (Fig. 1B column 1). Immunohistochemistry (IHC) staining demonstrated cytokeratin 10 (K10) and cytokeratin 14 (K14) expression in the suprabasal and basal layer, respectively, indicating properly differentiated epidermis resembling *in vivo* human skin architecture (Fig. 1B column 2) (43).

The antiviral screen was completed using two fluorescent markers; GFP-fused HSV-1 strain K26 (44) was employed to measure virus infection, while fibroblasts were transduced to constitutively express tdTomato to monitor compound cytotoxicity. The infection conditions were optimized by imaging the tissues using a high-content microscope at 24, 48, and 72 hours post-infection (HPI). The total fluorescence signal of GFP and tdTomato was quantitated using a maximum projection at a multiplicity of infection (MOI) of 0.1, 1.0, and 10 PFU/cell (Fig. 1C). GFP expression had the most significant difference between mock and infected using an MOI of 0.1 at 48HPI (difference in relative fluorescence units (ΔRFU) = 8753, $P < 0.001$), while the tdTomato signal was not affected (ΔRFU = 201.9, P = 0.8828) by viral infection (Fig. 1D). We applied these optimal infection conditions to subsequent experiments.

We used two different infection methods, the submerged and ALI skin tissues, to emulate infection routes during primary and recurrent viral encounters. The submerged culture maintained an undifferentiated single epithelium layer and was infected apically, resembling HSV primary infection at initial viral exposure. The ALI model included a stratified epidermis infected basolaterally, mimicking viral reactivation from the dermis. Submerged and ALI models were infected at MOI of 0.1 and imaged for quantification at 48HPI, GFP expression differed between the two models (Fig. 1E, columns 1 and 2). In the submerged model, apical infection of HSV-1 resulted in GFP expression mainly detected in keratinocytes above the tdTomato-positive dermal fibroblasts (Fig 1E, top row, column 2). In ALI cultures infected from the basolateral route of infection, there was colocalization of GFP and tdTomato signals, suggesting infection mainly occurred in the fibroblasts (Fig. 1E, bottom row, column 2). H&E and IHC staining demonstrated that infected submerged cultures had a disrupted epithelial monolayer, while infected ALI tissues maintained stratified epidermal morphology with proper K10 and K14 expression (Fig. 1E, columns 3 and 4). Since the submerged and ALI infection models preferentially targeted keratinocytes and fibroblasts, we used both models for anti-HSV drug screening.

To validate our screening assay pharmacologically, we tested acyclovir, the current standard of care for HSV, in dose-response in both submerged and ALI models (fig. S2). Acyclovir inhibited HSV-1 gene expression with minimal cytotoxic effects on the fibroblasts. However, the concentration of acyclovir required to achieve 50% inhibition of viral gene expression (IC_{50}) was > 9-fold lower in the ALI skin tissues ($IC_{50} < 0.04\mu M$) compared to the submerged tissues ($IC_{50} = 0.36\mu M$).

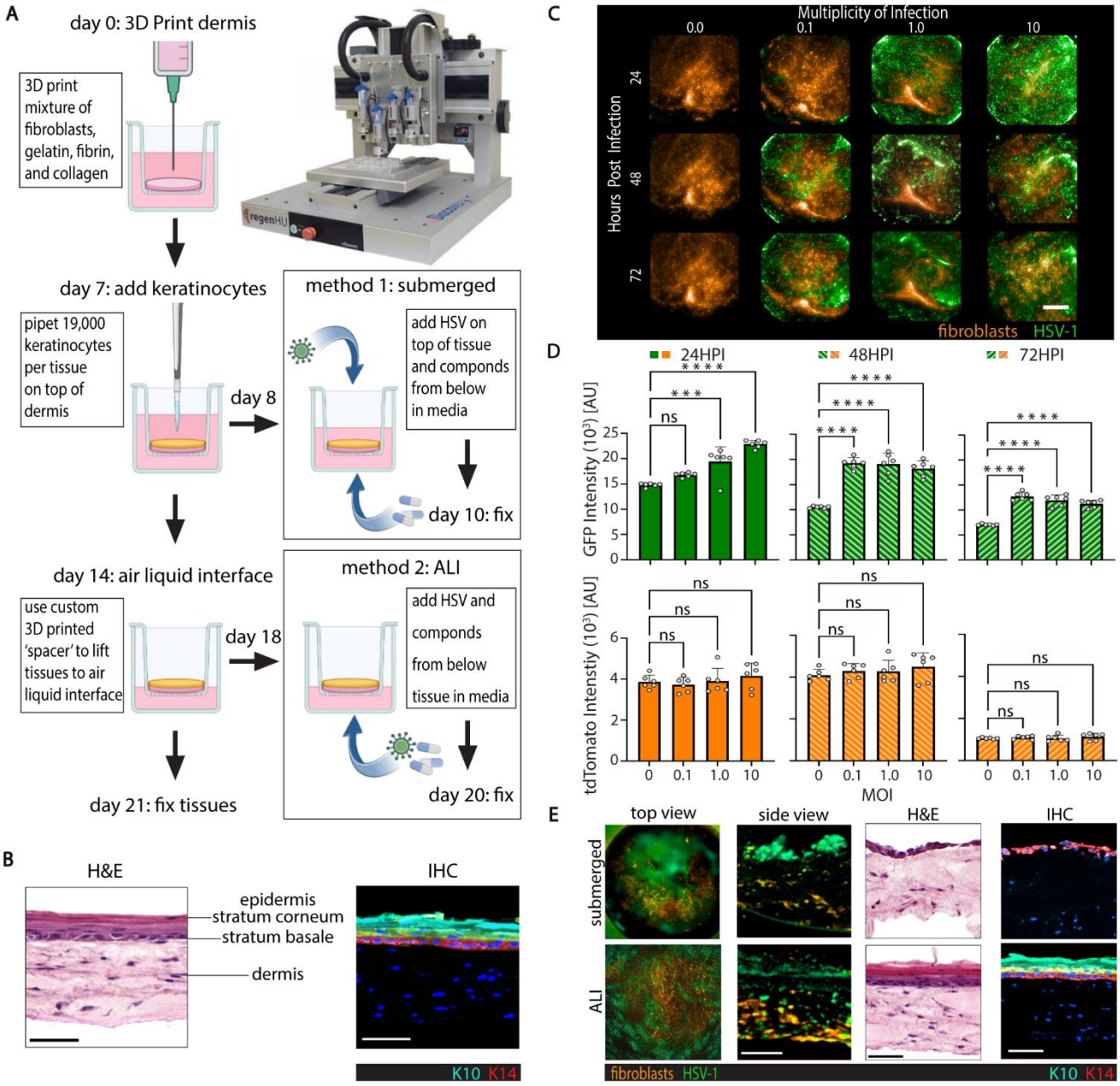

Fig. 1. 3D bioprinted HSE assay development and validation

(A) Dermis equivalents were 3D printed onto the apical side of transwell inserts using the RegenHU 3D Discovery bioprinter (image courtesy of RegenHU). Keratinocytes were pipetted onto the apical surface of the dermis. In the submerged model, the tissues were infected at the apical surface. In the ALI model, tissues were brought to ALI and then infected at the basolateral surface (created with BioRender.com). **(B)** H&E and IHC images of differentiated ALI tissues. K10 (cyan) and K14 (red) identify keratinocytes in the suprabasal and basal layer of the epidermis respectively (scale bar 50µm) **(C)** Submerged tissues were infected at various MOI and then imaged at specified times. Fibroblasts express tdTomato (orange) while infected cells express GFP (green) (scale bar 1mm). **(D)** GFP and tdTomato signal at each MOI and timepoint (*** $P < 0.001$, **** $P < 0.0001$ by ordinary one-way ANOVA). **(E)** Maximum projection of infected tissues from the top (column 1) or side (column 2) view. H&E (column 3) and IHC (column 4) staining of infected submerged or ALI models (scale bar 1mm (column 1) or 50µm (column 2, 3, 4).

2.2 Implementation of a Primary Drug Screen using 3D Bioprinted Human Skin Tissue Equivalents

We implemented a screen of 738 compounds with a wide range of mechanisms of action (MOA) (spreadsheet S1) utilizing our 3D bioprinted HSE assay platform. A primary screen tested the compound library in both the submerged and ALI infection models at 10μM compound concentration in duplicate, using 3,840 tissues. Each plate contained control wells: negative control (HSV-1 + DMSO), inhibitor control (media -HSV-1), and a known compound (HSV-1 + ACV (0.2μM)) (Fig. 2A). We used the maximum projection of each well to determine the total fluorescence of GFP (HSV-1 activity) and tdTomato (fibroblast viability) and normalized the data to the control wells in the corresponding test plate as described in Materials and Methods (Fig. 2B, fig. S3, spreadsheet S2).

To confirm the reproducibility of our assay, we compared the median GFP and tdTomato fluorescence signal from the negative control wells between the two assay repeats (n_1 vs n_2) in both the submerged and ALI models. The difference in the GFP or tdTomato intensity of the control wells was not significant in submerged models, indicating that our HSV-1 gene expression and fibroblast viability were consistent among all 32 plates (Fig. 2C, $P_{GFP} = 0.3045$, $P_{tdTomato} = 0.5641$). The difference in the GFP and tdTomato intensity of the control wells in the ALI plates was significant (Fig. 2C, $P_{GFP} = 0.0234$, $P_{tdTomato} = 0.0121$), emphasizing the need to normalize to include controls on each plate to correct for any variability.

To determine if our assay is amenable to HTS, we calculated the median *Z'*-factor, a measure of the robustness of the assay. A score that is Z'>0.5 denotes a robust assay window for screening, 0.5>Z'>0 indicates a marginal assay window and that the screen needs replicates, and a Z'<0 means that the assay window is not robust enough for screening. In the submerged model, the Z*'* was 0.57, and for the ALI model, the *Z'* was 0.13, indicating that the submerged assay has excellent robustness while the ALI assay has moderate robustness, demonstrating that our 3D bioprinted assay platform is amenable to HTS (fig. S4) (45). We identified 'hits' as compounds that inhibited GFP expression (HSV-1 activity) by at least 15% without causing more than 50%

reduction in tdTomato fluorescence (fibroblast viability) in either screen mode (Fig. 2D), selecting 106 compounds from the primary screen.

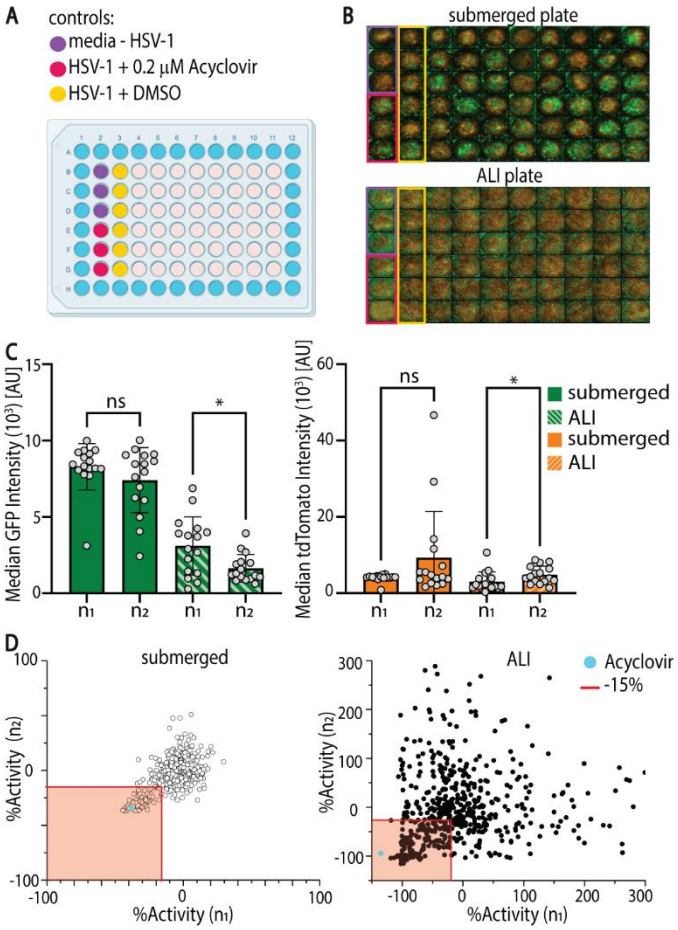

Fig. 2. Primary screen of compound library in 3D bioprinted assay platform
(A) Plate layout for compound screen. **(B)** Representative images from primary screen of submerged and ALI models. Controls are highlighted in boxes with colors corresponding to part (A). **(C)** Wilcoxon two-sample analysis of GFP intensity (left) and tdTomato intensity (right) of the median of the six negative control wells (HSV-1 + DMSO) across two replicate plates (n=16, * $P < 0.05$). **(D)** Correlation plots of replicates of primary screen of compounds. The red shaded box represents compounds that were selected as hits for re-testing if they reduced GFP expression (%Activity) by at least 15% in either replicate or model (left submerged, right ALI). The standard of care, acyclovir, was included in the collection and its activity is denoted by a cyan circle.

2.3 Secondary Drug Testing with 3D Bioprinted Human Skin Equivalents

Next, we performed a secondary screen of the 106 selected 'hits' in dose-response from 10µM to 0.04µM in the submerged and ALI models (spreadsheet S3). We found that 46% (submerged) and 70% (ALI) compounds reduced GFP expression (%Activity) by at least 50% at the maximum concentration tested without reducing tdTomato signal by 50% (%Viability) (Fig. 3A). Compounds tested were categorized by concentration-response curve (CRC) class (Fig. 3B) (45), according to their potency (IC_{50}) and efficacy (maximum percent activity). Compounds were considered candidate antivirals if they had CRC classes of -1.n or -2.n for HSV-1 inhibition

and CRC class of 4 for fibroblast viability in at least one infection model. Forty-one candidate antivirals were identified and grouped by MOA (Fig. 3C). The MOA clustering indicated that different mechanisms were more prevalent in each infection model. HDAC inhibitors (8%) and protease inhibitors (8%) were the prevalent candidates in the submerged model. DNA polymerase inhibitors (13%) were the prevalent antivirals in the ALI model (fig. S5). Inhibitors of proteasome, DNA polymerase, Casein Kinase 2, Exportin-1, GBF-1, and Ribonucleotide-Reductase were effective in both models. Of the 41 candidate antivirals, 23 are known or experimental HSV treatments (Fig. 3D), including five 'ciclovir' compound, the most common class of HSV antivirals (Fig. 3E, table S1) (46-66), demonstrating our assay's ability to identify HSV-1 antivirals in an unbiased screen..

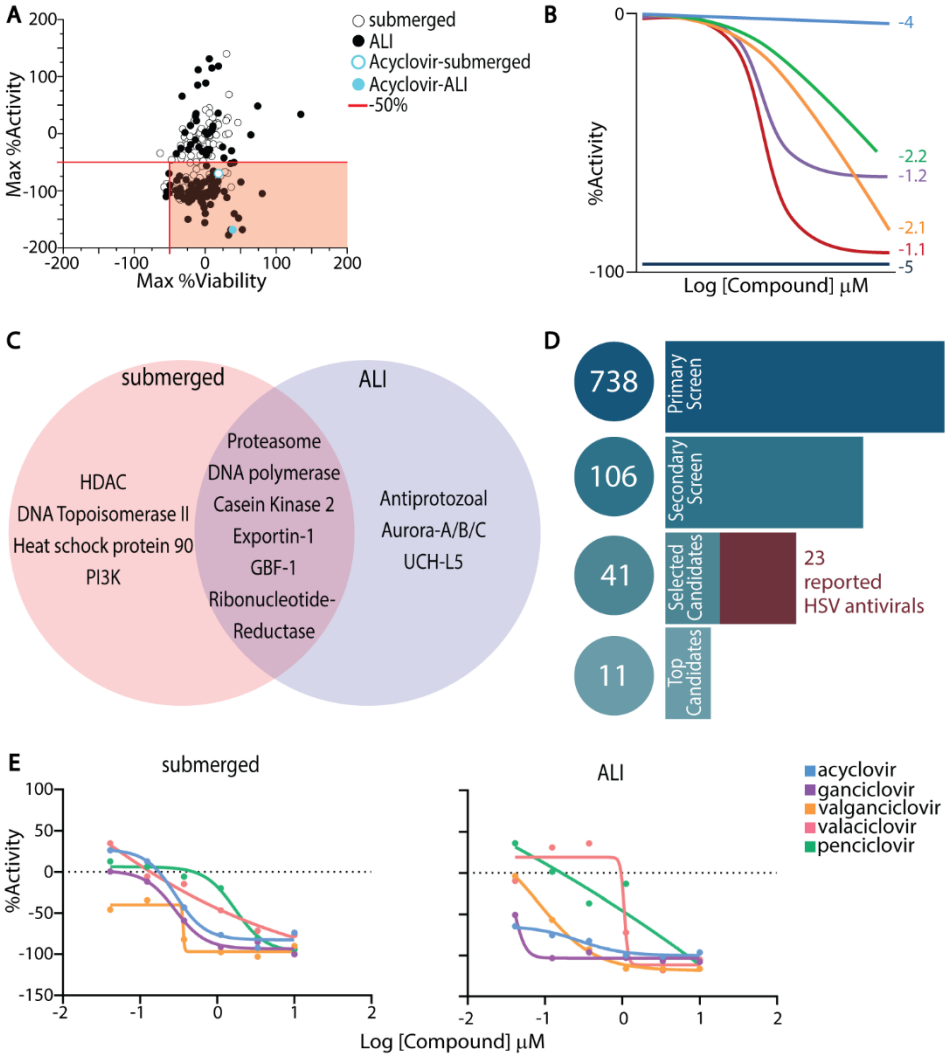

Fig. 3. Dose response of candidate antivirals in 3D bioprinted assay platform
(A) Correlation plot of Max %Activity (maximum reduction in GFP) vs. Max %Viability (maximum reduction in tdTomato) of 106 'hits' tested in dose response. Top candidate antivirals (50% or greater reduction in GFP) that did not kill over 50% of tdTomato transduced fibroblasts are identified by the red shaded box. **(B)** Schematic illustrating %Activity dose response profiles of different Concentration-Response Curve classes

(CRC). **(C)** Venn diagram showing divergent and coinciding targets for 41 top candidate antivirals in both submerged and ALI models. **(D)** Schematic of compounds selection from 738 compounds in the primary screen to 106 'hits' tested in dose-response to 41 selected candidates and 11 top candidates selected to move forward. Of the 41 selected candidates, 23 are current or experimental HSV treatments. **(E)** Dose response curves of candidate antivirals in "ciclovir" family, known to treat HSV-1, in submerged and ALI models.

We selected 11 of the 41 compounds as top candidate antivirals, including two known anti-herpes drugs, amenamevir and pritelivir (48, 52, 63), and four that have been reported to have anti-herpes activity: gemcitabine (58), lanatoside-C (60), niclosamide (54), and SNX-2112 (53). We re-tested these compounds in triplicate to assess potency and efficacy (Fig. 4A). IC_{50} (Fig. 4B) and maximum inhibition (Fig. 4C) indicate that compounds were generally more potent in the ALI than the submerged model in 10 of the 11 compounds tested (Table 1). The IC_{50} values were lower in the ALI model, from <0.04 to 0.22μM, compared to 0.05 to 6.67μM in the submerged model. Three compounds, fimepinostat, LDC4297, and VLX1570, showed significant differences in potency between the two models (Fig. 4B). We next plotted the viability of the tdTomato fibroblasts (Fig. 4D) and calculated the cytotoxic concentration required to kill 50% of target cells (CC_{50}) (Table 1). None of the compounds were cytotoxic in the ALI model; only three compounds, lanatoside-c, SNX-2112, and VLX1570, showed cytotoxicity in submerged models at higher concentrations.

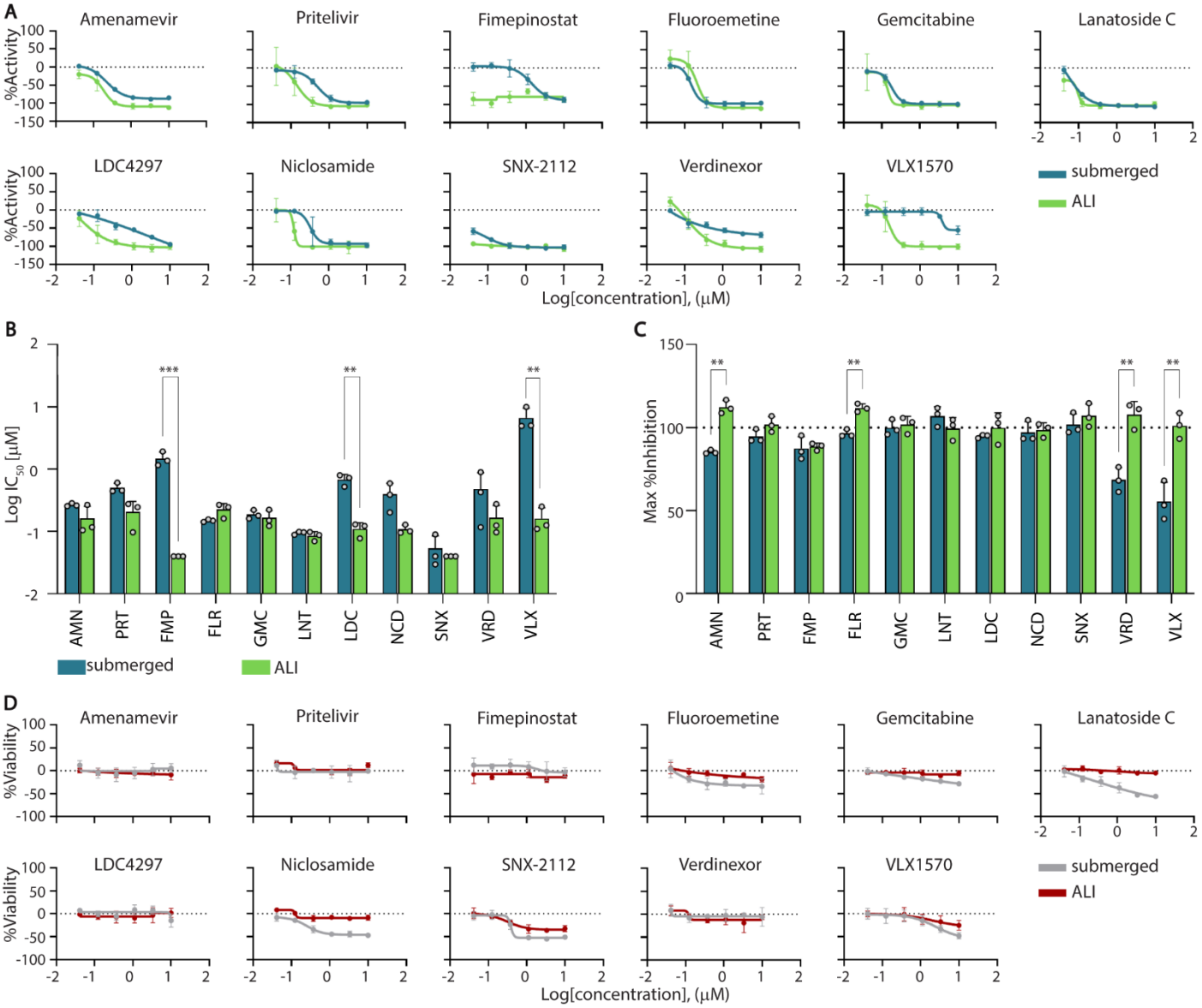

Fig. 4. Top candidate antiviral potency, efficacy, and cytotoxicity in 3D bioprinted HSE.
(A) Average dose-response curves for the 11 top candidate antivirals for submerged (blue) and ALI (green) models. **(B)** IC_{50} values for each top candidate antiviral compared between submerged (blue) and ALI (green) models. **(C)** Maximum inhibition for each top candidate antiviral compared between submerged (blue) and ALI (green) models. Statistical significance was determined by linear mixed model (*** $P < 0.001$, ** $P < 0.01$, * $P < 0.05$) for **(B)** and **(C)**. **(D)** CC_{50} dose response curves for 11 top candidate antivirals.

Candidate antiviral	Primary Mechanism of Action	Target	Submerged				ALI			
			Curve Class	Max Inhibition (%)	IC_{50} (μM)	CC_{50} (μM)	Curve Class	Max Inhibition (%)	IC_{50} (μM)	CC_{50} (μM)
Amenamevir (AMN)	Helicase primase inhibitor	Viral	-1.1	85.31	0.27	> 10	-1.1	112.36	0.16	> 10
Pritelivir (PRT)	Helicase primase inhibitor	Viral	-1.1	94.64	0.50	> 10	-1.2	101.90	0.21	> 10
Fimepinostat (FMP)	PI3K/HDAC inhibitor	Host	-1.1	87.43	1.48	> 10	-5	88.60	< 0.04	> 10
Fluoroemetine (FLR)	Unknown	Host	-1.1	96.50	0.15	> 10	-1.1	111.83	0.22	> 10
Gemcitabine (GMC)	Ribonucleotide Reductase	Host	-1.1	99.84	0.19	> 10	-1.2	101.78	0.16	> 10
Lanatoside C (LNT)	Autophagy inducer	Host	-1.1	106.86	0.09	2.49	-1.2	99.49	0.08	> 10
LDC4297 (LDC)	CDK inhibitor	Host	-2.1	94.82	0.68	> 10	-1.1	99.87	0.11	> 10
Niclosamide (NCD)	Multi-functional	Host	-1.1	97.13	0.39	> 10	-1.1	98.67	0.11	> 10
SNX-2112 (SNX)	HSP90 inhibitor	Host	-1.2	101.78	0.05	1.14	-5	107.14	< 0.04	> 10
Verdinexor (VRD)	Exportin Antagonist	Host	-1.3	68.57	0.48	> 10	-1.1	107.81	0.17	> 10
VLX1570 (VLX)	Protease deubiquitnase inhibitor	Host	-2.5	55.49	6.67	8.41	-1.1	101.22	0.16	> 10

Table 1: Pharmacologic profile of top candidate antivirals
Top candidate antivirals were selected from 41 compounds identified as potent and effective at doses below their respective CC_{50} in the primary and secondary screens. We re-tested these top candidate antivirals in triplicate and reported the Curve Class, Max Inhibition, IC_{50}, and CC_{50}. Known anti-HSV compounds, amenamevir and pritelivir, highlighted in grey.

2.4 Assessment of HSV Susceptibility and Acyclovir Antiviral Potency Across Different Cell Types

The primary and secondary screens identified that candidate antivirals exhibited different potency and efficacy in the submerged versus ALI model. Considering that keratinocytes were mainly infected in the submerged model in contrast to infected fibroblasts in the ALI model, we investigated how cell type could impact antiviral potency using 2D monocultures of primary skin cells and Vero cells, the cell line used to discover acyclovir (67). Keratinocytes and fibroblasts were isolated from 6 donors (table S2) using 3mm punch skin biopsies (Fig. 5A). Real-time monitoring of HSV-1 K26 infection via GFP fluorescence (fig. S6) revealed peak intensity at 20, 48, and 36 HPI in keratinocytes, fibroblasts, and Vero cells, respectively, (Fig. 5B&C). GFP expression (mean ± sd) increased exponentially 1.82 ± 0.51 hours earlier and 70.7 ± 36.9 % faster in keratinocytes than in fibroblasts ($P = 0.002$, fig. S7), indicating that HSV infection and viral gene expression occurred more rapidly in keratinocytes.

We then evaluated the potency and efficacy of acyclovir in a dose-dependent manner in donor-derived keratinocytes and fibroblasts (Fig. 5D). Dose-response curves were established using the previously determined peak infection time in each cell type (Fig. 5 E and F). All three cell types displayed similar dose responses using 20, 36, and 48 HPI (fig. S8). Acyclovir exhibited significant differences in potency between keratinocytes and fibroblasts across all six donors (Fig. 5D-G, $P < 0.001$). The IC_{50} of acyclovir (mean ± sd) was, on average, 176.4 ± 87.7-fold higher in keratinocytes (67.7± 18.2μM) than in fibroblasts (0.40 ± 0.2μM) and 57.5 ± 16.2-fold higher than in Vero cells (1.14 ± 0.2μM). The IC_{50} of acyclovir in keratinocytes was also over two-fold higher than published peak serum levels in patients following treatment with three times daily 1000mg valacyclovir (68). This suggests that current acyclovir treatment might not be optimal for inhibiting HSV gene expression in the skin epidermis. These results confirmed that the potency of antiviral drugs can vary substantially among cell types tested, emphasizing the importance of employing biologically relevant cells in antiviral drug testing to define their potency and efficacy.

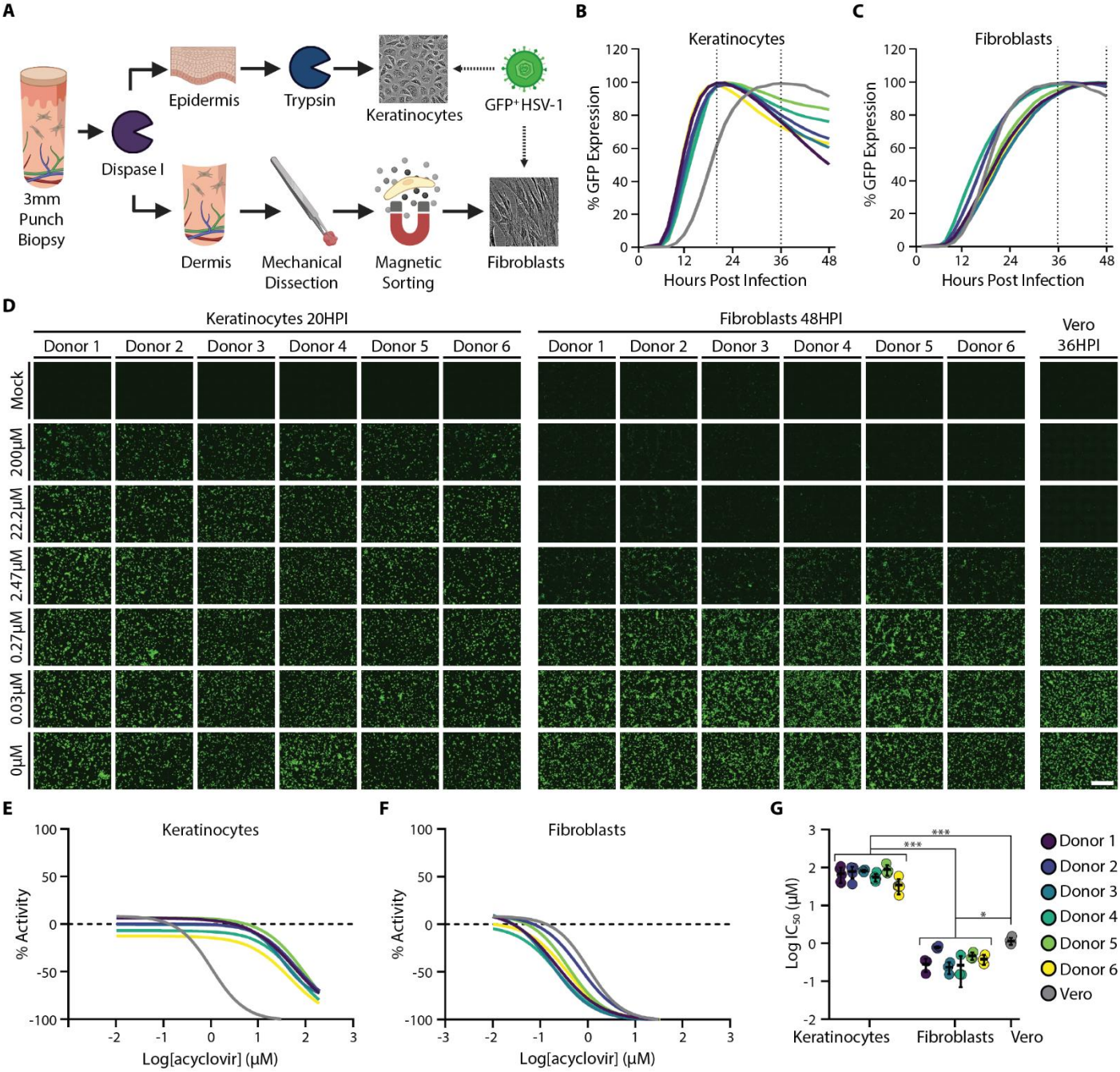

Fig. 5. Acyclovir potency in donor-derived primary keratinocytes and fibroblasts and in Vero cells. **(A)** Punch biopsies from six donors were collected and dissociated by enzymatic and mechanical processes. Vero cells, keratinocytes **(B),** and fibroblasts **(C)** were infected with GFP-expressing HSV-1, and live cell images were taken every two hours. **(D)** Keratinocytes, fibroblasts, and Vero cells were infected with GFP-expressing HSV-1 and then treated with acyclovir at the specified doses. Representative live cell images were taken at the peak of GFP expression. (Scale bar 500µm). **(E)** Dose-response curve of acyclovir in keratinocyte cultures compared to Vero cells (grey line). **(F)** Dose-response curve of acyclovir in fibroblast cultures compared to Vero cells (grey line). **(G)** IC_{50} values for each donor in each cell type (*** $P < 0.001$, * $P < 0.05$, linear mixed model).

2.5 Assessment of the Candidate Antiviral Activities in Donor-Derived Keratinocytes and Fibroblasts

We investigated the 11 top candidate antivirals in our 2D monocultures of donor-derived primary keratinocytes and fibroblasts in dose-response (Fig. 6A). According to the IC_{50} and maximum inhibition (Fig. 6B and C), all 11 candidate antivirals were 7 to >1050-fold more potent than acyclovir in keratinocytes, with IC_{50} values ranging from 0.07 to 9.9μM (Fig. 6, A and B, fig. S9). Five candidate antivirals, amenamevir, pritelivir, gemcitabine, lanatoside-C, and SNX-2112, surpassed acyclovir antiviral potency in fibroblasts as well, with IC_{50} values ranging from 0.05 to 0.15μM (Fig. 6A and B, fig. S10).

Antiviral potency differed significantly between keratinocytes and fibroblasts for 8 of the 12 compounds in donor-matched skin cells (Fig. 6B and C, fig. S11), although the differences were less than the difference seen in acyclovir (<27 fold versus >176 fold, respectively). Two notable exceptions were verdinexor and fimepinostat, which inhibited viral GFP expression by at least 50% in keratinocytes but failed to reliably inhibit viral GFP expression in fibroblasts. We also detected significant differences in keratinocytes, but not fibroblast, antiviral responses between donors 3 and 4 ($P < 0.001$) and donors 5 and 4 ($P = 0.02$) when considering potencies for all 11 compounds (fig. S12-14, table S3).

We next examined compound toxicity on keratinocytes and fibroblasts in the absence of viral infection (Fig. 6D, fig. S9&10). Keratinocytes were generally more sensitive to compound cytotoxicity than fibroblasts. Amenamevir and pritelivir, which target viral helicase/primase, showed a highly effective antiviral dosage (IC_{50} through IC_{80}) at >100-fold range lower than the CC_{50}, yielding a selectivity index of >250 in keratinocytes and >400 in fibroblasts (Fig. 6D, table S4). On the other hand, gemcitabine, SNX-2112, and lanatoside, which inhibit host pathways involving DNA replication, have high selective indexes (>750-1200) only in the fibroblasts and showed toxicity in keratinocytes.

Finally, we conducted a plaque reduction assay to confirm our candidate antivirals were effective against HSV-2 in addition to our findings with recombinant HSV-1. Primary keratinocytes in 6-well plates were infected with

either HSV-1 K26 or HSV-2 186 and treated with multiple doses of each candidate antiviral. All 11 candidate antivirals inhibited HSV-1 and HSV-2 plaque formation at similar doses (fig. S15).

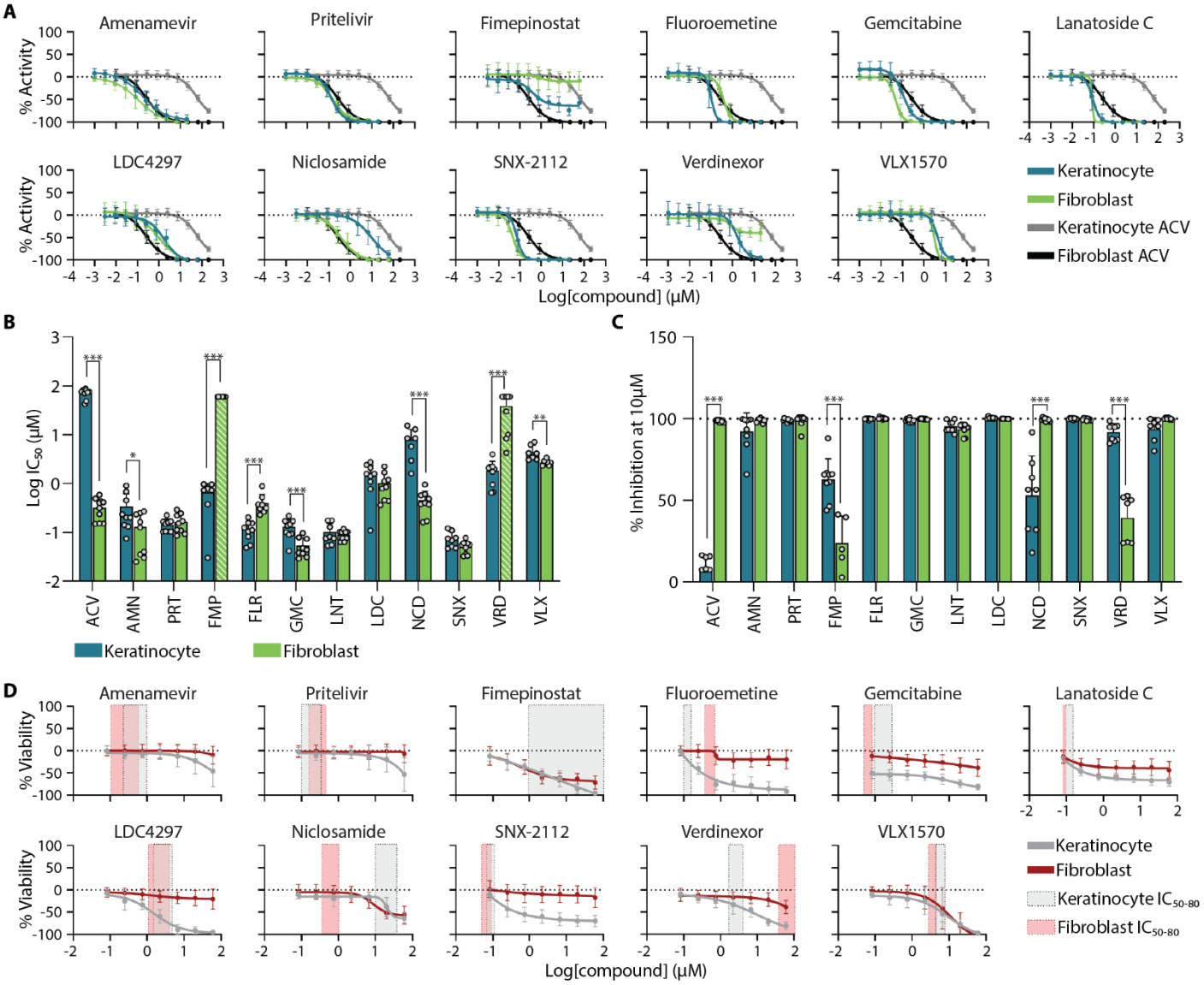

Fig. 6. Candidate antiviral potency, efficacy, and cytotoxicity in donor-derived primary keratinocyte and fibroblast monocultures.

(A) Dose-response curves for the 11 top candidate antivirals compared to acyclovir (ACV) (keratinocytes blue and grey, respectively; fibroblasts green and black, respectively). **(B)** IC_{50} values for each top candidate antiviral compared between keratinocytes (blue) and fibroblasts (green). Striped bars (FMP, VRD) indicate candidate antivirals that failed to reduce GFP expression by at least 50% consistently. **(C)** Maximum inhibition for each top candidate antiviral is compared between keratinocytes (blue) and fibroblasts (green). Statistical significance was determined by linear mixed model (*** $P < 0.001$, ** $P < 0.01$, * $P < 0.05$) for **(B)** and **(C)**. **(D)** CC_{50} dose-response curves for all twelve candidate antivirals compared to their respective IC_{50} to IC_{80} dose ranges. Keratinocyte data is from 20HPI (grey), while fibroblast data is from 48HPI (red).

2.6 Comparison of Candidate Antivirals in 2D Monoculture versus 3D Bioprinted Human Skin Equivalents

We compared the potency, toxicity, and selectivity index of the top 11 candidate compounds in our four models: 2D keratinocytes, 2D fibroblasts, 3D submerged, and 3D ALI (Fig. 7, A and B, table S5). The impact of cell type and 2D:3D model type on the antiviral potency was compound specific. Acyclovir was most significantly affected by cell type and the 2D:3D environment, whereas lanatoside C and SNX-2112 were unaffected (table S6). Submerged tissues and keratinocytes displayed more similar potencies than ALI tissues and fibroblasts, most likely due to the undifferentiated monolayer of keratinocytes infected in the submerged model (Fig. 7, C and D). Combining cell type differences between keratinocytes and fibroblasts and the 2D:3D growth environment, we showed that amenamevir, pritelivir, fluoroemetine, gemcitabine, lanatoside C, and SNX-2112 exhibited less than a 3-fold difference in average potency between models (Fig. 7C-E); all remaining candidate antivirals were >3-fold and more potent in the 3D model. Keratinocyte 2D monocultures were more susceptible to cytotoxic effects of candidate antivirals than 2D monocultures of fibroblasts or the 3D models, which identify toxicity through a loss of fluorescently labeled fibroblasts (Fig. 7B). All candidate compounds were selective (selectivity index >10) in the ALI model, and 9 of the 11 were selective in submerged models. While 8 of the 11 candidate antivirals were selective in 2D fibroblasts, only the two helicase-primase inhibitors were selective in 2D keratinocytes. Antiviral potency and toxicity can significantly differ between cell type and 2D:3D model tested, emphasizing the importance of applying physiologically relevant models to assess drug responses in early development *in vitro*.

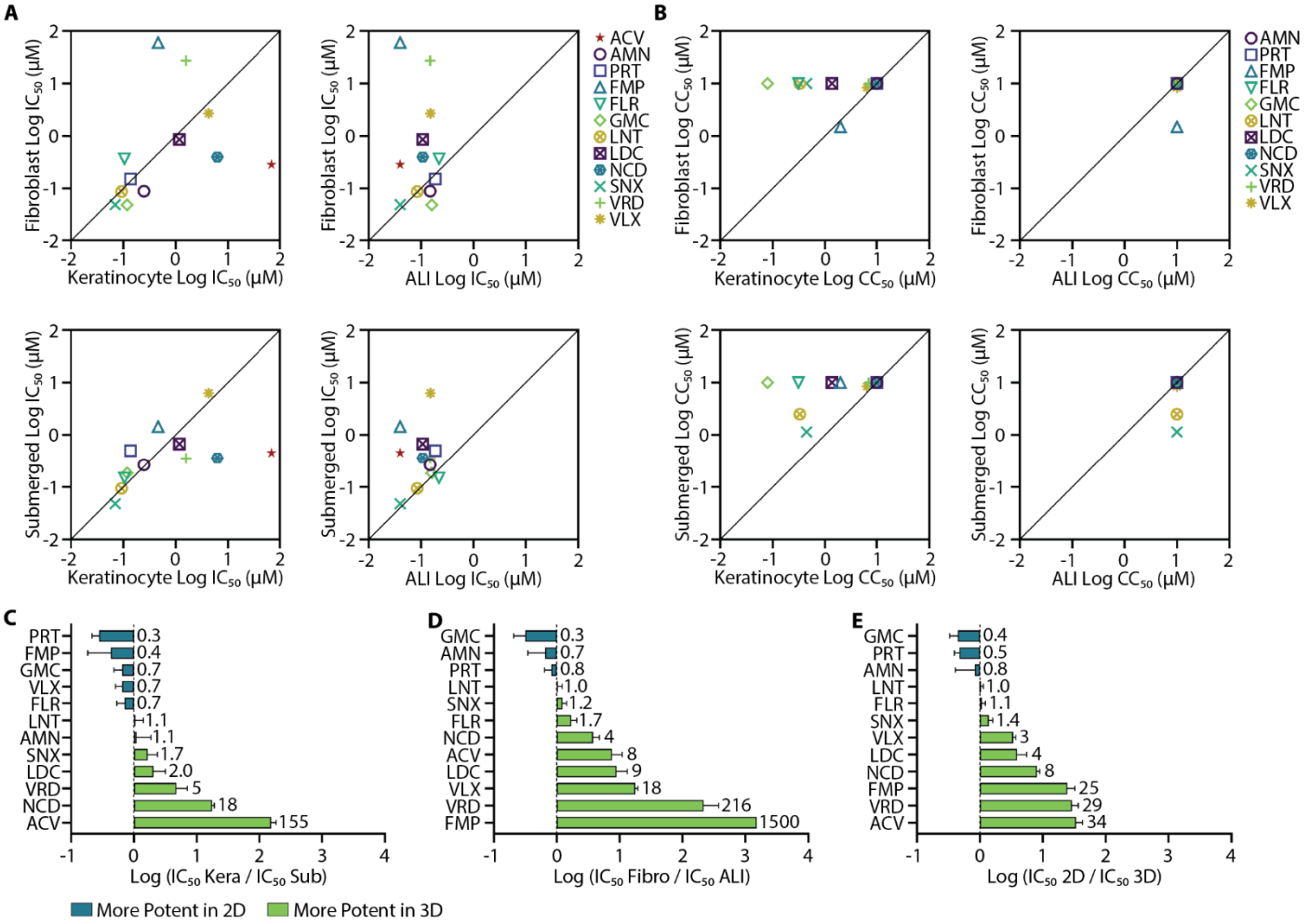

Fig 7: Comparison of 3D and 2D models in testing novel antiviral candidates.
(A) Pairwise comparisons of IC_{50} values for candidate antivirals in the four models tested. **(B)** Pairwise comparisons of CC_{50} values for candidate antivirals in the four models tested. **(C)** Fold change was determined by dividing the IC_{50} value of each candidate antiviral in keratinocytes by the IC_{50} of the same candidate antiviral in submerged models. **(D)** Fold change was determined by dividing the IC_{50} value of each candidate antiviral in fibroblasts by the IC_{50} of the same candidate antiviral in ALI models. **(E)** IC_{50} values for each candidate antiviral were pooled (keratinocytes and fibroblasts, submerged and ALI), then IC_{50} values for candidate antivirals in 2D were divided by IC_{50} values in 3D. **(C) (D) (E)** Green bars indicate candidate antivirals that were more potent in 3D, while blue bars indicate candidate antivirals that are potent in 2D.

2.7 Generation of 3D Bioprinted Human Skin Equivalents using Adult Donor-Derived Keratinocytes

Human neonatal skin cells are readily available commercially, but the ability to use adult donor-derived cells would increase the translational impact of our drug discovery assay platform. We bioprinted the dermis with commercial neonatal human dermal fibroblasts, then seeded the dermis with keratinocytes from donor 3 as a proof of concept to generate donor-specific HSE.

H&E staining of submerged and ALI HSE showed keratinocytes derived from donor 3 successfully developed into a stratified epidermis in the adult-derived ALI model with proper expression of K10 and K14 determined

by IHC (Fig 8, A and B). Of the 11 candidate antivirals, the majority displayed similar IC_{50} values in neonatal-derived and adult donor-derived HSE (Fig. 8, C and D). Four compounds in submerged models and three compounds in the ALI model were outside the 95% confidence interval (table S7). Thus, our assay platform can use easily accessible neonatal cells to investigate large numbers of compounds inexpensively, adult skin cells can then be utilized for further preclinical evaluation and enable drug testing in diverse genetic backgrounds.

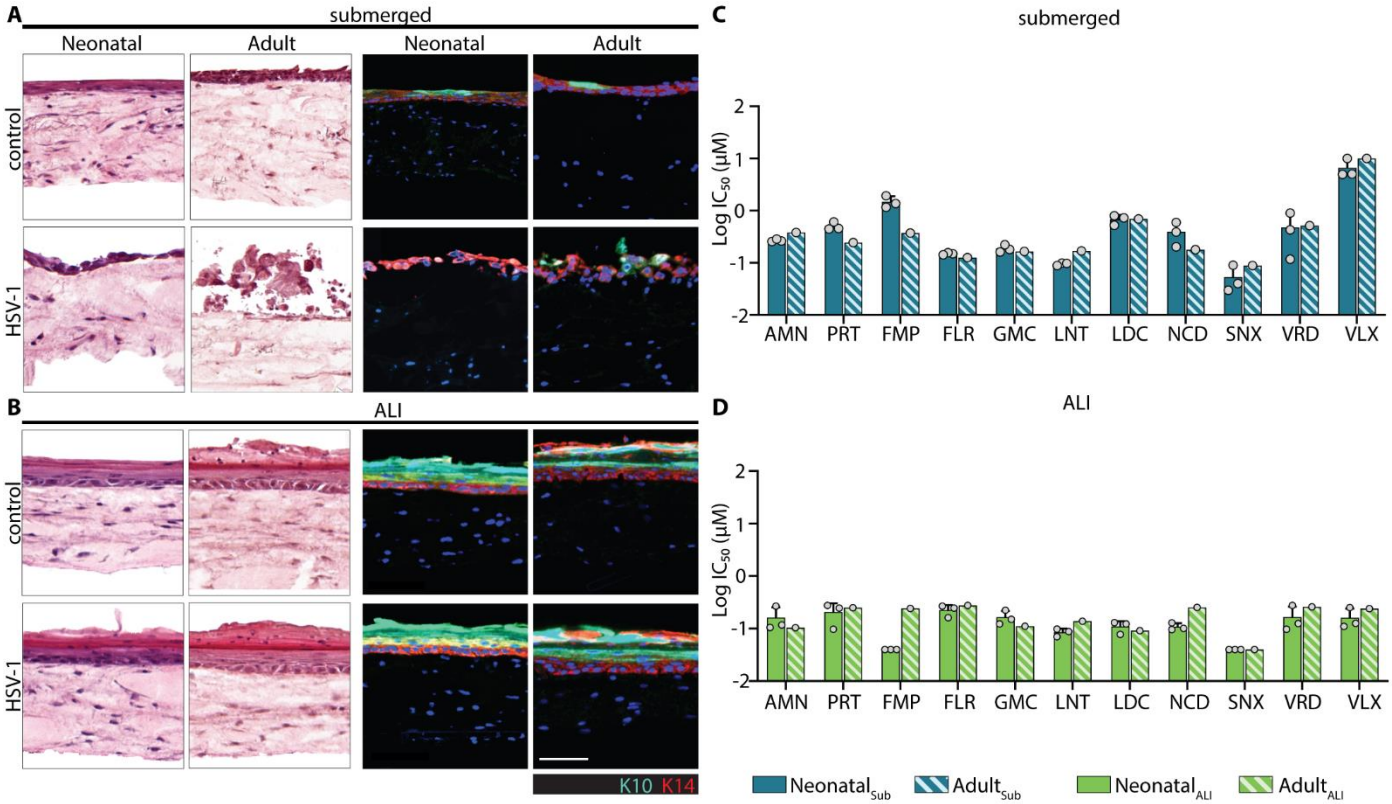

Fig 8: Generation of 3D bioprinted HSE using adult donor-derived keratinocytes
H&E and IHC staining of commercial neonatal or adult-derived bioprinted HSE in submerged **(A)** and ALI **(B)** models. Comparison of calculated IC_{50} in submerged **(C)** and ALI **(D)** models for top candidate antivirals.

DISCUSSION

We have employed a novel high-throughput assay leveraging 3D bioprinting to rapidly generate human skin equivalents (HSE) as an *in vitro* drug screening assay platform to identify potent HSV antiviral compounds. The 3D bioprinted HSE includes keratinocytes and fibroblasts in a multilayered architecture recapitulating the epidermis and dermis in an environment conducive to intercellular crosstalk, significantly impacting the infection pathway and pharmacological responses to compound treatments (69, 70). This automated 3D bioprinting process generated over 6,500 tissues in a 96-well format. GFP-expressing HSV-1 and tdTomato-expressing fibroblasts allowed our platform to rapidly screen potency, efficacy, and cytotoxicity for 738 distinct compounds. We identified 41 potential antiviral candidates; 23 of which are known or experimental HSV-1 antivirals, demonstrating the ability of our assay to identify active HSV antivirals in an unbiased screen. Employing adult human skin-derived keratinocytes and fibroblasts, we tested 11 top candidate antivirals and acyclovir for pharmacologic profiles using standard 2D monocultures. We demonstrated that the potency and efficacy of antiviral compounds can vary significantly between cell types and 2D versus 3D environments. The proof-of-concept application of successfully incorporating donor-derived adult cells incorporated into our platform to test antiviral responses expands the translational aspect of our preclinical drug screening platform.

Acyclovir, the standard of treatment for HSV infection, suppresses HSV lesion formation and reduces the ulcer lesion duration but fails to prevent the short episodes (<12 hours) of subclinical shedding (14, 15, 19). To our surprise, we showed that acyclovir was, on average, about 180-fold less potent in donor-derived primary keratinocytes, the main target of HSV infection in the skin, than matched fibroblasts. Further, the IC_{50} of acyclovir in these keratinocytes was over twice the peak clinical serum levels (68). Our data in 2D keratinocytes might explain why acyclovir fails to prevent asymptomatic shedding completely but likely overstates the IC_{50} for acyclovir in patients. Serum levels of acyclovir achieved with clinical doses may fail to control viral shedding completely, but they do significantly reduce symptomatic disease and viral load, indicating that the *in vivo* IC_{50} is likely lower than our results in 2D keratinocytes. In contrast, the 3D models still capture this cell type specific potency by indicating acyclovir is nearly 10-fold less potent in submerged models, which

predominantly features infected keratinocytes, but both 3D models align with clinical observations by indicating that acyclovir exhibits antiviral effects at doses below patient serum levels.

Our models also identified that targeting host cell mechanisms can lead to cell-type-specific antiviral effects. Targeting host mechanisms to develop antivirals has been employed for emerging pathogens, such as SARS-CoV-2 (71). Our data suggest that targeting host pathways may be limited for developing novel antivirals against all herpesviruses due to cell-type-specific differences. In contrast, antivirals that inhibit HSV helicase-primase, like amenamevir and pritelivir (48, 63), were highly selective in all 2D and 3D models tested and exhibited similar potencies in most models. The drugs that exhibited less than a 3-fold difference in potency for all models include pritelivir, amenamevir, gemcitabine, SNX-2112, fluoroemetine, and lanatoside C. Intriguingly, these first four of these drugs directly target viral DNA synthesis, while lanatoside C may prevent viral genetic material from entering the nucleus (48, 60, 63, 72, 73). Our data suggests that targeting the viral helicase-primase machinery is safe and effective, but drugs targeting the host cell replication machinery for DNA synthesis could be effective across multiple cellular environments as long as there is no toxicity issue. One exception to this paradigm is acyclovir. While acyclovir does inhibit viral DNA synthesis, it must first be processed by cellular thymidine kinase, which could provide a source of cell-type-specific variability (74). While targeting viral DNA synthesis was generally effective in all models tested, acyclovir provides a cautionary counterpoint that targeting these early stages of the viral lifecycle could still lead to cell-type-specific effects.

There are areas future iterations of our model can be improved. First, we could improve infection of stratified epithelium in the ALI culture through wounding at the apical surface to bypass the physical barrier of cornified epithelium (75). It’s not pursued in the current study due to difficulties in automating and standardizing the process in large screens, but it might be possible for later assays in top compounds. Second, our 3D models measure toxicity via tdTomato signal expressed by fibroblasts and did not capture keratinocyte toxicity. Future iterations of this model could incorporate a third fluorophore into keratinocytes to measure toxicity All 11 of

our candidate drugs effectively inhibited plaque formation by wildtype HSV-2 186 strain but constructing HSV-2 GFP expressing recombinant virus would benefit more direct and rapid testing against HSV-2 infection. Other strategies of antiviral drug development against wildtype and clinical isolates of HSV include modifying target cells to express GFP under a viral promoter.

Our assay platform can also be expanded by incorporating more donor-derived cells into our platform. Incorporation of broad genetic diversity in initial drug screening could improve clinical trial and patient outcomes if variable cellular factors heavily impact candidate drug efficacy (76). Our platform's ability to rapidly screen many different compounds could also be leveraged to screen combination therapy between a select group of compounds. Combination therapy could be used to overcome cell-type specific pharmaceutical properties or prevent the emergence of viral resistance, like the approach employed by antiretroviral therapy in treating HIV infection.

In summary, we have established a 3D bioprinted HSE assay platform that can be used for drug screening to identify anti-viral compounds in a high-throughput format. We demonstrated that potency and efficacy of candidate antivirals can vary significantly between cell types in both 2D cellular and 3D tissue cultures, with substantially lower potency observed for acyclovir in keratinocytes. Further, we identify that cell-type specific differences are largely absent in helicase-primase inhibitors, supporting the continued investigation of both this class of antivirals and novel antivirals targeting viral proteins. Finally, we establish that our assay platform can incorporate donor-derived cells, providing a way for early stages of drug discovery to include multiple donors with varied age, sex, ancestry, and genetic backgrounds to improve success in downstream clinical trials.

MATERIALS AND METHODS

Study Design

3D human skin equivalents (HSE) were generated in controlled experiments. Commercial neonatal fibroblasts and keratinocytes were expanded and frozen so that every experiment was performed at the same passage and using the same lot numbers. HSV-1 stocks were stored at -150°C and only used once to avoid freeze-thaw cycles. Candidate antivirals were spotted into 96 well receivers from the same stocks for all studies. Spotted plates were stored at -80°C and thawed on the day of use. All tissues were fixed at 48 hours post infection (HPI). Candidate antiviral wells were normalized to control wells, included on each plate. The primary screen was performed with duplicate biological repeats. The final 11 candidate antivirals were tested in dose-response with triplicate biological replicates. All submerged and ALI plates were processed using a circular mask to remove false fluorescent signal from the edge of the wells. We also applied a size-based background removal on the ALI plates. All background removal steps were performed before the fluorescence of each well was measured and data was normalized. The research goal of 3D tissue studies was to develop a method to measure HSV-1 infection, candidate antiviral activity, and candidate antiviral toxicity in 3D bioprinted HSE.

All 2D monoculture experiments were controlled laboratory experiments using low passage primary keratinocytes and fibroblasts. HSV-1 aliquots were used a single time without refreezing. All candidate antivirals were serially diluted in PBS from 10mM stocks in DMSO and stored as aliquots at -20°C. All candidate antivirals were tested in technical duplicate, and each cell type for each donor was tested in biological triplicate for each candidate antiviral. A biological replicate is classified as an independent experiment using different assay preparations. Individual wells from all live cell imaging experiments were manually confirmed to be clear of autofluorescent debris, such as plastic particles, which would erroneously impact IncuCyte identification of fluorescent signal. Wells with autofluorescent debris were excluded from analysis. The primary research objective for 2D monoculture was to compare candidate antiviral potency and efficacy between cell types and against 3D bioprinted HSE.

Statistical Analysis

Percent activity and percent viability in the 3D HSE was determined by normalizing the candidate antivirals to the control wells. Statistical analysis was completed using either Welch's two-tailed T-test or Wilcoxon two-sample test as described in figure legends.

Outliers in 2D monolayer studies were determined as values at least two logs higher than the mean. GFP fluorescence was normalized in 2D studies by subtracting fluorescence in mock infected wells and dividing by fluorescence in control untreated infected wells. Viability was determined in 2D studies by subtracting the total dead cells from the total cells to determine total live cells, then normalized by dividing the number of live cells in each experimental sample by the number of live cells in the 0.2% DMSO control at that timepoint. Statistical analysis for data sets involving multiple donors were analyzed by linear mixed models to account for donor to donor variability. Comparisons between submerged and ALI models were completed using linear models as a single cell source was used for all 3D tissues. Fold change calculations with 2D and 3D models used geometric means to account for the large differences between values.

Commercial Cell Culture and Transduction:

Neonatal human dermal fibroblasts (HDF_N, Zen Bio DFN-F) were cultured in Dulbecco's Modified Eagle Medium (DMEM, Gibco 11965) supplemented with 10% Fetal Bovine Serum (FBS) and 1% penicillin streptomycin. The fibroblasts were fluorescently labeled by transduction with lentiviral particles for fluorescent whole-cell labeling with tdTomato expression (Takara 0037VCT). A solution of polybrene and lentivirus at 20 multiplicities of infection (MOI) was added to the flask for 4 hours at 37°C, then virus solution was removed, and cells were expanded for 10 days, then frozen. Neonatal Normal Human Epithelial Keratinocytes ($NHEK_N$, ScienCell 2100) were cultured in KBM Gold basal medium (Lonza, Cat. # 00192151) supplemented with the KGM Gold Keratinocyte Growth Medium BulletKit (Lonza, Cat. #00192152). All cell types were incubated at 37°C and 5% CO_2.

Donor Procured Primary Cell Isolation and Culture:

This study was approved by the University of Washington Institutional Review Board. All primary cells were collected under IRB approval STUDY00004312. Written informed consent was collected from all participants.

Primary cell culture was completed using matched donor cells from 3mm punch biopsies collected as previously described (77). All cell culture medium contained 25mg streptomycin (Gibco 15140-122) and 25,000 units Penicillin (Gibco 15140-122). Keratinocytes were grown on collagen coated plates (Corning 35440) using DermaCult basal medium (Stem Cell Technologies 100-0501) with DermaCult keratinocyte expansion supplements (100-0502), 38µg Hydrocortisone (Stem Cell Technologies 07925), and 125µg Amphotericin B (Gibco 15290-019) added. The keratinocyte culture medium was supplemented with 10µM of the Rho Kinase inhibitor Y-27632 dihydrochloride (Stem Cell 72304) for the first six days after collection (78). Fibroblasts were grown on standard uncoated tissue culture vessels using Fibroblast Basal Medium 2 (PromoCell C-23220) with Fibroblast Growth Medium 2 supplement pack (PromoCell C-39320). All cells were maintained at 37°C in a humidified incubator under 5% CO_2.

Preparation of Dermal Base Hydrogel:

Gelatin powder (Sigma G1890, final concentration 0.045mg/mL) was dissolved in a fibrinogen solution (Sigma F3879, final concentration 7.7mg/mL) in PBS, at 37°C. After complete dissolution of the gelatin, collagen I (Corning 354249, final concentration 4mg/mL) was added, and the solution was mixed thoroughly. 10X phosphate-buffered saline (PBS, Invitrogen AM9624) was added to buffer the gelatin/fibrinogen/collagen solution. The mixture was kept at 37°C and neutralized with 1N NaOH immediately before adding the fibroblasts.

Fibroblasts at 70% confluence were dissociated, harvested from the flask, counted with a Countess II FL hemocytometer, and then centrifuged at 650x g for 4 minutes. The pellet was resuspended in ~10mL of the Dermal Base Hydrogel, at 2 million cells per mL, and mixed well by gentle pipetting. The solution was loaded

into a 10mL syringe (Hamilton 81620) and chilled in the fridge for ~5 minutes. Finally, a 0.42mm ID luer lock needle tip (Nordson 7018263) was placed on the syringe and the syringe was loaded onto the RegenHU 3DDiscovery bioprinter.

3D Printing the Dermal Bioink:

A plunger-based bioprinting system was used to extrude the dermal base hydrogel solution in a cylindrical-crosshatched pattern made up of two 0.25mm thick layers with a diameter of 4.2mm directly on top of the membrane (8µm pore-size PET) of an HTS Transwell 96-well Permeable Support Plate (transwell plate, Corning 3374). The extrusion pattern was designed with the RegenHU BioCAD Software. To minimize evaporation effects, the hydrogel was not printed in any edge wells. After bioprinting was complete, the transwell was placed on a receiver plate filled with 250mL of serum-free DMEM supplemented with 5units/mL thrombin (Sigma T6884) at RT to allow the fibrinogen-fibrin conversion. After 1 hour, media in the receiver plates was changed to DMEM medium supplemented with 10% FBS, 1% penicillin streptomycin, and 0.025mg/mL aprotinin (Sigma A4529). The plates were incubated at 37°C and 5% CO_2; media was replaced every 48 hours.

Addition of Keratinocytes:

7 days after bioprinting the dermal base, keratinocytes ($NHEK_N$) at 70% confluence were dissociated, harvested from the flask, counted using a hemocytometer, pelleted at 650x g for 4 minutes, then resuspended in KGM medium at 0.4 million cells per mL. 50µL of the keratinocyte suspension (20,000 cells) was pipetted on top of the 3D bioprinted dermal base. Media in the receiver plates was changed to 250µL of epidermalization medium per well supplemented with 0.025mg/mL aprotinin (40). The plates were incubated at 37°C and 5% CO_2; media was replaced every 48 hours.

Air-Liquid Interface:

7 days after adding the keratinocytes, the ALI model tissues were lifted to air liquid interface (ALI) using a custom 3mm high 3D printed adaptor made of SBS-format compliant material. The adaptor lifted the transwell insert, leaving only the bottom of the dermal base in contact with the media while the top of the tissues was exposed to air. The media in the receiver plate was replaced with 510µL of cornification medium supplemented with 0.025mg/mL aprotinin (40). Plates were incubated at 37°C and 5% CO_2; media was replaced every 48 hours.

HSV Infection in 3D Bioprinted HSE:

All viral infection experiments utilized a GFP-expressing recombinant HSV-1 strain, K26 (44). To infect bioprinted HSE, HSV-1 stocks were thawed over ice for ~1 hour then diluted in media for the submerged infection method or cornification media for the ALI infection method. The optimal MOI of HSV-1 for infection assays in the 3D bioprinted HSE was determined by diluting HSV-1 in cell growth media to 0.1, 1.0, and 10 MOI, then adding the virus onto the apical side of the submerged tissues one day after seeding keratinocytes. Z-stacks were captured at 4X magnification on an inverted microscope, and a maximum projection was used to quantitate GFP and tdTomato total fluorescence signal of each well at 24, 48, and 72 hours post infection (HPI). In the subsequent antiviral screening experiments, we used the HSV-1 at 0.1 MOI and fixed tissues at 48HPI.

We implemented two methods of infecting the 3D bioprinted HSE for antiviral screening. In the submerged method, the virus and the antivirals were added to the tissues one day after seeding the keratinocytes to the dermal base. The tissues were infected on the apical surface, but compounds were added to the media on the basal side of the tissues. In the ALI model, the virus and compounds were both added to the media on the basal side of the tissue four days after lifting to ALI to mimic viral reactivation.

Compound Plate Preparation:

For the screen, compounds were spotted into a 96-well receiver plates with the drug solutions at the appropriate stock concentrations in DMSO and frozen at -80°C until ready for use. The plate map used for the screen is shown in Figure 3A, with controls included on each plate including an inhibitor control (media -HSV-1), a negative control (HSV-1 + DMSO), and a known compound (HSV-1 + 0.2µM acyclovir).

Histology:

Tissues were fixed in 4% Paraformaldehyde for 24 hours then soaked in 30% sucrose for 24 hours at 4°C. The tissues were cut out from the transwell plate with a scalpel then embedded in Scigen Tissue Plus O.C.T. Compound (Fisher Scientific 23-730-571) at -20°C. The embedded tissues were sliced in 10µm sections with a CryoStar NX50 then mounted on positively charged slides. H&E staining was performed on the ThermoFisher Gemini stainer using the predefined H&E protocol. Using the Bond Fully Automated IHC Staining System, tissues were stained for primary antibodies keratin 10 and keratin 14 with Akoya Opal secondaries in 690 and 520 respectively. Slide images were taken in 10X with the Leica Aperio Versa 200.

Imaging and Data Normalization of 3D Printed Tissues:

Tissues were fixed in 4% Paraformaldehyde for 24 hours before washing with PBS. Fluorescent images were taken with a Molecular Devices ImageXpress High Content Reader using a 4X objective and excitation and emission wavelengths of 475-650nm for GFP and 544-570nm for tdTomato. Z-stacks of the images were taken at 25µm step size and a maximum Z-projections were made for each well using the MetaXpress Image Analysis.

The fluorescent signal for each tissue was measured using the MetaXpress Image Analysis software. To remove the fluorescent signal of the well edges, a circular mask of ~4mm in diameter was created and only signal within the ‘circle mask’ was measured. For the ALI tissues an additional step was included to decrease background autofluorescence signal; a size-based inclusion threshold of 14.8µm or more was used to measure

'cell-sized' objects. (fig. S3) For both models, the GFP and tdTomato fluorescence intensity from the z-stack maximum projection was measured for each well. The intensity values were then normalized to the high and low signal controls using the equation:

$$\%activity = 100\ x\ \frac{c-n}{n-i}$$

where *c* is the candidate antiviral fluorescence intensity value, *n* is the median signal from the negative controls (HSV-1 + DMSO), and *i* is the median signal of the inhibition control (media -HSV-1) for the GFP signal and 0 for the tdTomato signal.

Analysis of 3D model applicability for high throughput screening

The reproducibility of results obtained using both the submerged and ALI 3D models was determined by Z-score, which was calculated using the following equation (45):

$$Z' = \frac{(AVG_{max} - \frac{3SD_{max}}{\sqrt{n}}) - (AVG_{min} - \frac{3SD_{min}}{\sqrt{n}})}{AVG_{max} - AVG_{min}}$$

where AVG_{max}=negative control (HSV-1 + DMSO) and AVG_{min} =inhibitor control (media -HSV-1), SD_{max} and SD_{min} is the standard deviation of the negative and inhibitor control respectively, and *n* is the number of wells in each control group (45).

2D monoculture candidate antiviral testing:

Primary keratinocytes were seeded in collagen coated 96 well plates (Revvity 6005810) and used at passage number six or less. Primary fibroblasts from the same keratinocyte donors were seeded in standard 96 well plates (Revvity 6005182) and used at passage number eight or less. 2D monocultures were infected with K26 HSV-1 using a MOI of 1.0 in serum free medium. Cells were infected at time zero and incubated on a rocker at 37°C and 5% CO_2 for one hour prior to drug administration. Plates were imaged every two hours using a 10X objective on an IncuCyte S3/SX1. All images collected were analyzed using the IncuCyte software version

2021B (Sartorius). Infected wells treated with the 0.2% DMSO control were used to determine positive fluorescent signal while uninfected wells were used to determine background fluorescence for automated analysis. GFP expression is displayed as integrated intensity, defined as the total increase in fluorescent intensity as a function of the total area of detectable fluorescence.

Cytotoxicity was determined in the absence of HSV infection by treating cells with specified doses of candidate antivirals and using a combination of membrane permeable NucSpot Live 488 dye (Biotium 40081) and membrane impermeable NucSpot 594 dye (Biotium 41037). The cytotoxicity dose response curve was determined at 20 hours post treatment (HPT) for keratinocytes and 48 HPT for primary fibroblasts to align with IC_{50} timepoints.

Plaque Reduction Assay

6-well plates (Corning 3516) were coated with 0.04mg/mL collagen I (Corning 354236) diluted in filter sterilized 0.1% acetic acid (VWR UN2789) for 1 hour, then seeded with primary keratinocytes. 95% confluent keratinocyte cultures were infected the next day using 40 plaque forming units of either HSV-1 K26 or HSV-2 186. Cells were infected at time zero and incubated on a rocker at 37°C and 5% CO_2 for one hour prior to drug administration. DermaCult was prepared as described above then supplemented with 1% methylcellulose and candidate antivirals at the required concentrations. Excess virus was removed after one hour and replaced with overlay media containing candidate antivirals. Plaques were allowed to develop for 72 hours at 37°C and 5% CO_2, then cells were fixed for 30 minutes in 4% paraformaldehyde (product code) and stained with crystal violet (product code) before manual counting.

IncuCyte IC_{50} Calculations:

All IC_{50} values were determined by GraphPad Prism 9 using integrated fluorescent intensity of GFP measured by the IncuCyte software. IC_{50} values were calculated at 20, 36, or 48 HPI as specified. Uninfected wells served as the negative control and were used as the minimum signal (0%), while drug-free infected wells were used as

the positive control and represent the maximum signal (100%). IC_{50} was calculated using a four parameter least squares nonlinear regression comparing the drug concentration to normalized response.

References

1. Looker KJ, Magaret AS, May MT, Turner KM, Vickerman P, Gottlieb SL, et al. Global and Regional Estimates of Prevalent and Incident Herpes Simplex Virus Type 1 Infections in 2012. PLoS One. 2015;10(10):e0140765.
2. Looker KJ, Magaret AS, Turner KM, Vickerman P, Gottlieb SL, Newman LM. Global estimates of prevalent and incident herpes simplex virus type 2 infections in 2012. PLoS One. 2015;10(1):e114989.
3. Gupta R, Warren T, Wald A. Genital herpes. Lancet. 2007;370(9605):2127-37.
4. James SH, Kimberlin DW. Neonatal Herpes Simplex Virus Infection. Infect Dis Clin North Am. 2015;29(3):391-400.
5. Corey L, Wald A, Celum CL, Quinn TC. The effects of herpes simplex virus-2 on HIV-1 acquisition and transmission: a review of two overlapping epidemics. J Acquir Immune Defic Syndr. 2004;35(5):435-45.
6. Freeman EE, Weiss HA, Glynn JR, Cross PL, Whitworth JA, Hayes RJ. Herpes simplex virus 2 infection increases HIV acquisition in men and women: systematic review and meta-analysis of longitudinal studies. AIDS. 2006;20(1):73-83.
7. Abu-Raddad LJ, Magaret AS, Celum C, Wald A, Longini IM, Jr., Self SG, et al. Genital herpes has played a more important role than any other sexually transmitted infection in driving HIV prevalence in Africa. PLoS One. 2008;3(5):e2230.
8. Zhu J, Hladik F, Woodward A, Klock A, Peng T, Johnston C, et al. Persistence of HIV-1 receptor-positive cells after HSV-2 reactivation is a potential mechanism for increased HIV-1 acquisition. Nat Med. 2009;15(8):886-92.
9. Looker KJ, Welton NJ, Sabin KM, Dalal S, Vickerman P, Turner KME, et al. Global and regional estimates of the contribution of herpes simplex virus type 2 infection to HIV incidence: a population attributable fraction analysis using published epidemiological data. Lancet Infect Dis. 2020;20(2):240-9.
10. Stanberry LR, Spruance SL, Cunningham AL, Bernstein DI, Mindel A, Sacks S, et al. Glycoprotein-D-adjuvant vaccine to prevent genital herpes. N Engl J Med. 2002;347(21):1652-61.
11. Bernstein DI, Cardin RD, Bravo FJ, Strasser JE, Farley N, Chalk C, et al. Potent adjuvant activity of cationic liposome-DNA complexes for genital herpes vaccines. Clin Vaccine Immunol. 2009;16(5):699-705.
12. Cohen J. Immunology. Painful failure of promising genital herpes vaccine. Science. 2010;330(6002):304.
13. Belshe RB, Leone PA, Bernstein DI, Wald A, Levin MJ, Stapleton JT, et al. Efficacy results of a trial of a herpes simplex vaccine. N Engl J Med. 2012;366(1):34-43.
14. Kaufman HE, Heidelberger C. Therapeutic Antiviral Action of 5-Trifluoromethyl-2'-Deoxyuridine in Herpes Simplex Keratitis. Science. 1964;145(3632):585-6.
15. King DH. History, pharmacokinetics, and pharmacology of acyclovir. J Am Acad Dermatol. 1988;18(1 Pt 2):176-9.
16. Kit S, Sheppard M, Ichimura H, Nusinoff-Lehrman S, Ellis MN, Fyfe JA, et al. Nucleotide sequence changes in thymidine kinase gene of herpes simplex virus type 2 clones from an isolate of a patient treated with acyclovir. Antimicrob Agents Chemother. 1987;31(10):1483-90.
17. Bacon TH, Levin MJ, Leary JJ, Sarisky RT, Sutton D. Herpes simplex virus resistance to acyclovir and penciclovir after two decades of antiviral therapy. Clin Microbiol Rev. 2003;16(1):114-28.
18. Sauerbrei A, Deinhardt S, Zell R, Wutzler P. Phenotypic and genotypic characterization of acyclovir-resistant clinical isolates of herpes simplex virus. Antiviral Res. 2010;86(3):246-52.
19. Johnston C, Saracino M, Kuntz S, Magaret A, Selke S, Huang ML, et al. Standard-dose and high-dose daily antiviral therapy for short episodes of genital HSV-2 reactivation: three randomised, open-label, cross-over trials. Lancet. 2012;379(9816):641-7.
20. Celum C, Wald A, Hughes J, Sanchez J, Reid S, Delany-Moretlwe S, et al. Effect of aciclovir on HIV-1 acquisition in herpes simplex virus 2 seropositive women and men who have sex with men: a randomised, double-blind, placebo-controlled trial. Lancet. 2008;371(9630):2109-19.
21. Celum C, Wald A, Lingappa JR, Magaret AS, Wang RS, Mugo N, et al. Acyclovir and transmission of HIV-1 from persons infected with HIV-1 and HSV-2. N Engl J Med. 2010;362(5):427-39.

22. Eungdamrong NJ, Higgins C, Guo Z, Lee WH, Gillette B, Sia S, et al. Challenges and promises in modeling dermatologic disorders with bioengineered skin. Exp Biol Med (Maywood). 2014;239(9):1215-24.
23. Esch EW, Bahinski A, Huh D. Organs-on-chips at the frontiers of drug discovery. Nat Rev Drug Discov. 2015;14(4):248-60.
24. Ekert JE, Deakyne J, Pribul-Allen P, Terry R, Schofield C, Jeong CG, et al. Recommended Guidelines for Developing, Qualifying, and Implementing Complex In Vitro Models (CIVMs) for Drug Discovery. SLAS Discov. 2020;25(10):1174-90.
25. Schmook FP, Meingassner JG, Billich A. Comparison of human skin or epidermis models with human and animal skin in in-vitro percutaneous absorption. Int J Pharm. 2001;215(1-2):51-6.
26. Mak IW, Evaniew N, Ghert M. Lost in translation: animal models and clinical trials in cancer treatment. Am J Transl Res. 2014;6(2):114-8.
27. Pound P, Bracken MB. Is animal research sufficiently evidence based to be a cornerstone of biomedical research? BMJ. 2014;348:g3387.
28. Scannell JW, Blanckley A, Boldon H, Warrington B. Diagnosing the decline in pharmaceutical R&D efficiency. Nat Rev Drug Discov. 2012;11(3):191-200.
29. Avorn J. The $2.6 billion pill--methodologic and policy considerations. N Engl J Med. 2015;372(20):1877-9.
30. DiMasi JA, Grabowski HG, Hansen RW. Innovation in the pharmaceutical industry: New estimates of R&D costs. J Health Econ. 2016;47:20-33.
31. Gopallawa I, Gupta C, Jawa R, Cyril A, Jawa V, Chirmule N, et al. Applications of Organoids in Advancing Drug Discovery and Development. J Pharm Sci. 2024.
32. Bhatia SN, Ingber DE. Microfluidic organs-on-chips. Nat Biotechnol. 2014;32(8):760-72.
33. Huh D, Hamilton GA, Ingber DE. From 3D cell culture to organs-on-chips. Trends Cell Biol. 2011;21(12):745-54.
34. Gauglitz GG, Schauber J. Skin: Architecture and Function. In: Kamolz L-P, Lumenta DB, editors. Dermal Replacements in General, Burn, and Plastic Surgery: Tissue Engineering in Clinical Practice. Vienna: Springer Vienna; 2013. p. 1-11.
35. Briggaman RA, Wheeler CE, Jr. The epidermal-dermal junction. J Invest Dermatol. 1975;65(1):71-84.
36. Sun S, Jin L, Zheng Y, Zhu J. Modeling human HSV infection via a vascularized immune-competent skin-on-chip platform. Nat Commun. 2022;13(1):5481.
37. Bell E, Ehrlich HP, Buttle DJ, Nakatsuji T. Living tissue formed in vitro and accepted as skin-equivalent tissue of full thickness. Science. 1981;211(4486):1052-4.
38. Lee V, Singh G, Trasatti JP, Bjornsson C, Xu X, Tran TN, et al. Design and fabrication of human skin by three-dimensional bioprinting. Tissue Eng Part C Methods. 2014;20(6):473-84.
39. Abaci HE, Guo Z, Doucet Y, Jackow J, Christiano A. Next generation human skin constructs as advanced tools for drug development. Exp Biol Med (Maywood). 2017;242(17):1657-68.
40. Derr K, Zou J, Luo K, Song MJ, Sittampalam GS, Zhou C, et al. Fully Three-Dimensional Bioprinted Skin Equivalent Constructs with Validated Morphology and Barrier Function. Tissue Eng Part C Methods. 2019;25(6):334-43.
41. Liu X, Michael S, Bharti K, Ferrer M, Song MJ. A biofabricated vascularized skin model of atopic dermatitis for preclinical studies. Biofabrication. 2020;12(3):035002.
42. Gangatirkar P, Paquet-Fifield S, Li A, Rossi R, Kaur P. Establishment of 3D organotypic cultures using human neonatal epidermal cells. Nat Protoc. 2007;2(1):178-86.
43. Ling-juan Z. Keratins in Skin Epidermal Development and Diseases. In: Miroslav B, editor. Keratin. Rijeka: IntechOpen; 2018. p. Ch. 5.
44. Desai P, Person S. Incorporation of the green fluorescent protein into the herpes simplex virus type 1 capsid. J Virol. 1998;72(9):7563-8.
45. Iversen PW BB, Chen YF, Dere W, Devanarayan V, Eastwood BJ, Farmen MW, Iturria SJ, Montrose C, Moore RA, Weidner JR, Sittampalam GS. HTS Assay Validation. 2012. In: Assay Guidance Manual [Internet] [Internet]. Bethesda, MD: Eli Lily & Company and the National Centers for Advancing Translational Research. Available from: https://www.ncbi.nlm.nih.gov/books/NBK83783/.
46. Taylor M, Gerriets V. Acyclovir. StatPearls. Treasure Island (FL)2024.

47. De Clercq E. Clinical potential of the acyclic nucleoside phosphonates cidofovir, adefovir, and tenofovir in treatment of DNA virus and retrovirus infections. Clin Microbiol Rev. 2003;16(4):569-96.
48. Chono K, Katsumata K, Kontani T, Kobayashi M, Sudo K, Yokota T, et al. ASP2151, a novel helicase-primase inhibitor, possesses antiviral activity against varicella-zoster virus and herpes simplex virus types 1 and 2. J Antimicrob Chemother. 2010;65(8):1733-41.
49. Wyler E, Franke V, Menegatti J, Kocks C, Boltengagen A, Praktiknjo S, et al. Single-cell RNA-sequencing of herpes simplex virus 1-infected cells connects NRF2 activation to an antiviral program. Nat Commun. 2019;10(1):4878.
50. Schneider SM, Pritchard SM, Wudiri GA, Trammell CE, Nicola AV. Early Steps in Herpes Simplex Virus Infection Blocked by a Proteasome Inhibitor. mBio. 2019;10(3).
51. Ushio C, Ariyasu H, Ariyasu T, Arai S, Ohta T, Fukuda S. Suppressive effects of a cyanine dye against herpes simplex virus (HSV)-1 infection. Biomed Res. 2009;30(6):365-8.
52. Kleymann G, Fischer R, Betz UA, Hendrix M, Bender W, Schneider U, et al. New helicase-primase inhibitors as drug candidates for the treatment of herpes simplex disease. Nat Med. 2002;8(4):392-8.
53. Preston CM, Rinaldi A, Nicholl MJ. Herpes simplex virus type 1 immediate early gene expression is stimulated by inhibition of protein synthesis. J Gen Virol. 1998;79 (Pt 1):117-24.
54. Andersen PI, Krpina K, Ianevski A, Shtaida N, Jo E, Yang J, et al. Novel Antiviral Activities of Obatoclax, Emetine, Niclosamide, Brequinar, and Homoharringtonine. Viruses. 2019;11(10).
55. La Frazia S, Amici C, Santoro MG. Antiviral activity of proteasome inhibitors in herpes simplex virus-1 infection: role of nuclear factor-kappaB. Antivir Ther. 2006;11(8):995-1004.
56. Trousdale MD, Nesburn AB, Watanabe KA, Fox JJ. Evaluation of the antiherpetic activity of 2'-fluoro-5-iodo-ara-C in rabbit eyes and cell cultures. Invest Ophthalmol Vis Sci. 1981;21(6):826-32.
57. Poole CL, James SH. Antiviral Therapies for Herpesviruses: Current Agents and New Directions. Clin Ther. 2018;40(8):1282-98.
58. Denisova OV, Kakkola L, Feng L, Stenman J, Nagaraj A, Lampe J, et al. Obatoclax, saliphenylhalamide, and gemcitabine inhibit influenza a virus infection. J Biol Chem. 2012;287(42):35324-32.
59. Tan D. Potential role of tenofovir vaginal gel for reduction of risk of herpes simplex virus in females. Int J Womens Health. 2012;4:341-50.
60. Wu S, Wang S, Lin X, Yang S, Ba X, Xiong D, et al. Lanatoside C inhibits herpes simplex virus 1 replication by regulating NRF2 distribution within cells. Phytomedicine. 2024;124:155308.
61. Ishimaru H, Hosokawa K, Sugimoto A, Tanaka R, Watanabe T, Fujimuro M. MG132 exerts anti-viral activity against HSV-1 by overcoming virus-mediated suppression of the ERK signaling pathway. Sci Rep. 2020;10(1):6671.
62. Huang Q, Hou J, Yang P, Yan J, Yu X, Zhuo Y, et al. Antiviral activity of mitoxantrone dihydrochloride against human herpes simplex virus mediated by suppression of the viral immediate early genes. BMC Microbiol. 2019;19(1):274.
63. Betz UA, Fischer R, Kleymann G, Hendrix M, Rubsamen-Waigmann H. Potent in vivo antiviral activity of the herpes simplex virus primase-helicase inhibitor BAY 57-1293. Antimicrob Agents Chemother. 2002;46(6):1766-72.
64. Xiang YF, Qian CW, Xing GW, Hao J, Xia M, Wang YF. Anti-herpes simplex virus efficacies of 2-aminobenzamide derivatives as novel HSP90 inhibitors. Bioorg Med Chem Lett. 2012;22(14):4703-6.
65. Carmine AA, Brogden RN, Heel RC, Speight TM, Avery GS. Trifluridine: a review of its antiviral activity and therapeutic use in the topical treatment of viral eye infections. Drugs. 1982;23(5):329-53.
66. Spruance SL, Tyring SK, DeGregorio B, Miller C, Beutner K. A large-scale, placebo-controlled, dose-ranging trial of peroral valaciclovir for episodic treatment of recurrent herpes genitalis. Valaciclovir HSV Study Group. Arch Intern Med. 1996;156(15):1729-35.
67. Elion GB, Furman PA, Fyfe JA, de Miranda P, Beauchamp L, Schaeffer HJ. Selectivity of action of an antiherpetic agent, 9-(2-hydroxyethoxymethyl) guanine. Proc Natl Acad Sci U S A. 1977;74(12):5716-20.
68. Lycke J, Malmestrom C, Stahle L. Acyclovir levels in serum and cerebrospinal fluid after oral administration of valacyclovir. Antimicrob Agents Chemother. 2003;47(8):2438-41.
69. El Ghalbzouri A, Lamme E, Ponec M. Crucial role of fibroblasts in regulating epidermal morphogenesis. Cell Tissue Res. 2002;310(2):189-99.

70. Wang Z, Wang Y, Farhangfar F, Zimmer M, Zhang Y. Enhanced keratinocyte proliferation and migration in co-culture with fibroblasts. PLoS One. 2012;7(7):e40951.
71. Zhou Y, Hou Y, Shen J, Huang Y, Martin W, Cheng F. Network-based drug repurposing for novel coronavirus 2019-nCoV/SARS-CoV-2. Cell Discov. 2020;6:14.
72. Ciccolini J, Serdjebi C, Peters GJ, Giovannetti E. Pharmacokinetics and pharmacogenetics of Gemcitabine as a mainstay in adult and pediatric oncology: an EORTC-PAMM perspective. Cancer Chemother Pharmacol. 2016;78(1):1-12.
73. Qin S, Hu X, Lin S, Xiao J, Wang Z, Jia J, et al. Hsp90 Inhibitors Prevent HSV-1 Replication by Directly Targeting UL42-Hsp90 Complex. Front Microbiol. 2021;12:797279.
74. Miller WH, Miller RL. Phosphorylation of acyclovir diphosphate by cellular enzymes. Biochem Pharmacol. 1982;31(23):3879-84.
75. De La Cruz NC, Mockel M, Wirtz L, Sunaoglu K, Malter W, Zinser M, et al. Ex Vivo Infection of Human Skin with Herpes Simplex Virus 1 Reveals Mechanical Wounds as Insufficient Entry Portals via the Skin Surface. J Virol. 2021;95(21):e0133821.
76. Li J, Zhang L, Zhou H, Stoneking M, Tang K. Global patterns of genetic diversity and signals of natural selection for human ADME genes. Hum Mol Genet. 2011;20(3):528-40.
77. Henrot P, Laurent P, Levionnois E, Leleu D, Pain C, Truchetet ME, et al. A Method for Isolating and Culturing Skin Cells: Application to Endothelial Cells, Fibroblasts, Keratinocytes, and Melanocytes From Punch Biopsies in Systemic Sclerosis Skin. Front Immunol. 2020;11:566607.
78. Terunuma A, Limgala RP, Park CJ, Choudhary I, Vogel JC. Efficient procurement of epithelial stem cells from human tissue specimens using a Rho-associated protein kinase inhibitor Y-27632. Tissue Eng Part A. 2010;16(4):1363-8.

Acknowledgements

This work was supported by NIH funding AI143773 and TR003208 to JZ, T32 AI07140 to IRH, and NIH

Intramural Research Program and Cure Acceleration Network Program to NCATS.